# Geant4 Simulation for the Responses of X-rays and Charged Particles through Wolter-type Focusing Mirrors

L.Q. Qi,[1] G. Li,[1] J. Zhang,[1] Y.P. Xu,[1] F.J. Lu,[1] S. Basso,[2] R. Campana,[3] Y. Chen,[1] A. De Rosa,[3] G. Pareschi,[2] P.F. Qiang,[4] A. Santangelo,[5] L.Z. Sheng,[4] G. Sironi,[2] L.M. Song,[1] G. Tagliaferri,[2] J. Wang,[1] J. Wilms,[6] Y.J. Yang,[1] and Y. Zhang[1]

[1] *Key Laboratory of Particle Astrophysics, Institute of High Energy Physics, Chinese Academy of Sciences, Beijing 100049, China*
[2] *INAF-Brera Astronomical Observatory, Via E. Bianchi 46, 23807 Merate, Italy*
[3] *INAF/IASF, Via del Fosso del Cavaliere 100, I-00133Roma, Italy*
[4] *XIOPM, Xi'an Institute of Optics and Precision Mechanics, CAS, NO.17 Xinxi Road, Xi'an, Shaanxi, China*
[5] *Institut für Astronomie und Astrophysik Tübingen, Sand 1, 72076 Tübingen, Germany*
[6] *Remeis Observatory & ECAP, Universität Erlangen-Nürnberg, Sternwartstr. 7, 96049 Bamberg, Germany*

The geometric and physical models of Wolter-I type mirrors have been developed based on Geant4, which can simultaneously simulate the mirror responses of X-ray and charged particles. It is used to better design the payloads of the enhanced X-ray Timing and Polarimetry observatory (eXTP). A new geometry class G4Hyperboloid is created and validated, which allows an exact surface profile description of Wolter-I optics. The physical model for the interaction of X-rays and matters is extended to effectively estimate the focusing performances with reasonable accuracy, including effective area and point spread function. Scattering models of charged particles in grazing incidence are discussed. Multiple scattering models are demonstrated to have the capability to reproduce the funnelling effect with reasonable accuracy and CPU cost, when the step size is properly constrained. In the end, a preliminary design of magnetic diverter is performed, as an example of the application based on the mirror responses.

## I. INTRODUCTION

The enhanced X-ray Timing and Polarimetry observatory is a space mission aiming to study physics under extreme conditions [1]. It carries several types of instruments to study X-rays in the energy range of 0.5-30 keV. Two types of the instruments implement Wolter-I optics to focus and imagine X-rays, namely spectroscopy focusing array (SFA) and polarimetry focusing array (PFA). The mirror performances are crucial for the detailed design of payloads, including the mirror responses of X-rays and charged particles. The X-ray focusing performances have great impact on the sensitivity of focal plane detectors (FPDs). On the other hand, Wolter-I type optics behave like a concentrator for charged particles, inducing additional background and radiation damage to FPDs. In order to evaluate the performances and optimize the design of eXTP, it is essential to describe the mirror response of X-rays and charged particles in detail with reasonable accuracy.

The simulation of the mirror responses of X-rays and charged particles is usually performed with separate models and tools. The design of an optical system is a complex task. Various physical models and ray-tracing codes are dedicated for such kind of tasks [2, 3], e.g. ZEMAX, Q and WISE. In addition, optical physics can be incorporated into Geant4 [4] as external module to simulate the interaction between X-rays and matters [5–7]. For example, a generic ray-tracing toolbox XRTG4 based on Geant4 has been developed to reproduce the measured effective area with accuracy about 5% and the main properties of point spread function (PSF), with simplified geometry and X-ray scattering model [5].

Wolter-I type mirror is designed to focus X-rays, but it can also concentrate charged particles onto FPDs, namely the funnelling effect. It has drawn attention since the launch of XMM-Newton and Chandra, on which significant performance degradation of FPDs was observed due to an increase of charge transfer inefficiency (CTI) [8, 9]. The physical mechanism behind the funnelling effect is still not clear. Various physical models [10–16] have been proposed in the last few years. The funnelling effect was firstly explained such that a proton undergoes numerous scattering in layer, deflected from its original direction, and finally escapes the layer. Several multiple scattering models and single scattering model have been investigated in case of grazing incidence, indicating that single scattering model has the best possible accuracy [17, 18]. Numerical solutions, which give the angular distribution of the scattered protons, have also been used for the explanation of the funnelling effect [17–20], including the Firsov model and elastic Remizovich model.

In this work, the exact geometrical model of the mirror is established, and the physical models are extended in the same simulation framework of Geant4. The X-ray response of the mirror is described in section II. The possible physical mechanisms behind the funneling effect are discussed in section III, followed by their mirror responses. The mirror response of X-rays and charged particles can be used as input data for detailed design of the payloads. An example of magnetic diverter design for protons is provided in section IV.

## II. X-RAY RESPONSE

A ray-tracing model based on Geant4 is developed in this work. The main purpose is to quickly estimate the overall achievable performances for X-rays in Wolter-I optics, i.e. effective area and imaging quality. In this section, the geometrical and the physical models are described, followed by corresponding validation and results.

### A. Geometrical and Physical Models

Two types of the instruments of eXTP are equipped with Wolter-I [21] optics to focus and imagine X-rays. The optics consist of a parabolic (primary segment) and a hyperbolic surface (secondary segment) with grazing-incidence reflection. In the current mirror configurations of eXTP, the optics have a focal length of 5.25 m and a field of view (FOV) of $8'$, dedicated for the photon energy range between 0.5 keV and 10.0 keV. The length of the optics is 600 mm including primary and secondary segments and the aperture radius ranges from 112 mm to 238 mm. The preliminary design comprises 45 mirror shells, which adopts Nickel substrate and Gold reflective coatings. A schematic view of the nested confocal mirrors can be seen in figure 1.

Geant4 10.5 geometry library does not provide possible description for hyperbolic surfaces. So the Wolter-I mirror profile was usually approximated by double-cone or many consecutive conical segments in simulations [5]. In this work, a new geometry G4Hyperboloid is implemented in Geant4 toolkit, realizing an exact geometric description of Wolter-I type mirrors together with G4Paraboloid class. The main advantage of this work is that the geometric aberration due to double-cone approximation can be fully eliminated. The half energy width (HEW), i.e. angular diameter collecting 50% of photons, is usually used to characterize the angular resolution of the imaging system. This quantity can be directly obtained from the fractional encircled energy function (EEF), defined as the fraction of the total energy in the point spread function, see figure 2. The on-axis HEW for a double-cone profile with perfectly smooth surface is $45.84''$ in the current mirror configurations, which is already larger than the scientific requirements of the mission (typically $30''$). In fact, the perfect parabolic-hyperbolic profile of Wolter-I mirror has no intrinsic aberration on-axis. Thus an exact geometric description ensures the accuracy of the subsequent simulation and also simplifies the implementation of the physical and statistical models that represent the effects of the surface roughness.

The imaging quality of mirror depends on not only the intrinsic properties but also many other effects, including aperture diffraction, mirror shape accuracy, surface finishing level, mounting and alignment error etc. Provided the energy range of X-ray (above 0.5 keV) interested for the mission, the aperture diffraction has negligible effects on the angular resolution [2, 3, 22]. The PSF broadening effect is then mainly due to the differences between the real and perfect shape of the mirror surfaces. The differences are usually classified into figure error and microroughness depending on the spatial scale of the geometric irregularities. Even though the boundary between the two regimes is not known priori, the figure error typically corresponds to large spatial scale, while microroughness is usually due to the spatial scale close to or smaller than the wavelength of photons. The model in this work considers figure error of large spatial scale plus microroughness effect.

Figure errors with large spatial scale can be treated by geometric optics, where photon is perfectly reflected in a mirror-like way and the local surface normal is tilted at a very small scale. For each photon impinges on the reflective layer, the efficiency is determined by the Fresnel reflectivity as a function of the photon energy and incident angle [23]. It is calculated by the Fresnel equation with complex index of refraction, whose value can be approximated by anomalous dispersion theory or obtained from the data libraries of Center for X-ray Optics (CXO) [24]. The angle of reflection equals to the incident angle with respect to the local surface normal, whose direction gets

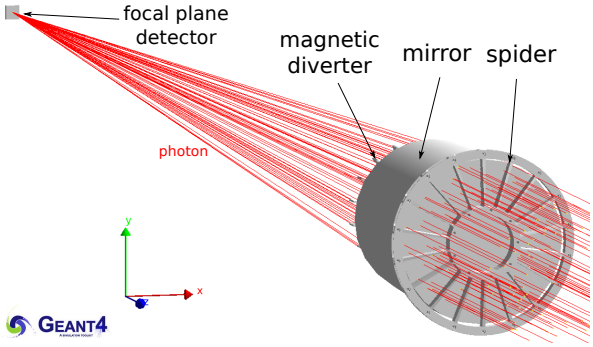


FIG. 1. Schematic view of the nested confocal Wolter-I type mirror of eXTP.

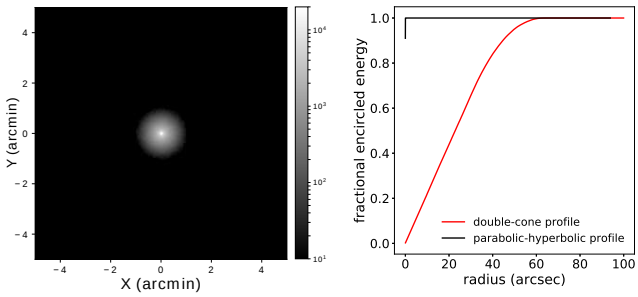


FIG. 2. On-axis PSF for double-cone mirror profile with perfectly smooth surface (left). On-axis EEF function for double-cone profile and parabolic-hyperbolic profile with perfectly smooth surface, respectively (right).

tilted with the presence of large-scale deformations. The perturbation function of local surface normal for each interaction can use either a random distribution [25] or certain mirror profile [26].

When the spatial scale is smaller and gets close to the wavelength of the photon, geometric optics is not applicable any more since the photons should be treated as waves. The photons are scattered in all directions due to diffraction, also known as X-ray scattering (XRS). The fraction of scattered photons obeys the well-known Debye-Waller formula [27]:

$$\frac{I_s}{I_0} = 1 - e^{-\frac{16\pi^2\sigma^2\sin^2\theta_i}{\lambda^2}} \tag{1}$$

where $\sigma$ is the microroughness, $\lambda$ the photon wavelength and $\theta_i$ the grazing-incidence angle. The scattered intensity per radian within the smooth surface limit follows [2]:

$$\frac{dI_s}{d\theta_s} = \frac{16\pi^2}{\lambda^3}\sin\theta_i\sin^2\theta_s\frac{1}{2}P(f) \tag{2}$$

$$f = \frac{\cos\theta_i - \cos\theta_s}{\lambda} \tag{3}$$

where P(f) is the power spectral density (PSD) of the surface, f the spatial frequency and $\theta_s$ the scattering angle. Different PSD formula based on the surface finishing level can be used, e.g. a power-law approximation [28] $P(f) = K_n/f^n$. It is obvious that the XRS is energy dependent and sensitive to the shape of PSD, especially at high-frequency domain.

The physics process of photons and matter in grazing-incidence is implemented in Geant4 by means of boundary process. The process is invoked once a photon from vacuum reaches a pre-defined reflective surface. All the information of particles (energy and momentum) and geometries (surface normal) are easily accessed directly from the toolkit. Then the change of photons based on the selected scattering model is invoked for each track.

### B. Validation

The ray-tracing model in Geant4 is validated in terms of effective area and angular resolution. For effective area, the comparison between simulation and analytical calculation is performed in figure 3 for one mirror shell. At each energy, $10^6$ photons are simulated in Geant4 to limit the statistical error. The well-known analytical formula is used for the estimation of effective area both on-axis and off-axis, for an astronomical source at infinity [29]:

$$A_\infty(\lambda,\theta) = 4R_0L\int_0^{\pi/2}(\alpha_0 - \theta\cos\varphi)r_\lambda(\alpha_1)r_\lambda(\alpha_2)d\varphi \tag{4}$$

where $\theta$ is the off-axis angle, $R_0$ the radius at the intersection plane, L the length of the mirror segment (here the primary segment length $L_1$ equals to secondary segment length $L_2$), $\alpha_0$ the incident angle at the intersection plane, $\varphi$ the azimuthal angle and r the reflectivity. The incident angle in the primary and secondary segments can be estimated, for a small off-axis angle $\theta$ and an astronomical source at infinity, as following:

$$\alpha_1(\varphi) \simeq \alpha_0 - \theta\cos\varphi \tag{5}$$

$$\alpha_2(\varphi) \simeq \alpha_0 + \theta\cos\varphi \tag{6}$$

The comparison shows good agreement both on-axis and off-axis in terms of the the peak positions and the overall shape, see figure 3. The observed discrepancy is probably due to the assumption used to deduce the analytical formalism [29]. Nevertheless, the discrepancy is within 3% in the whole energy range. Thus the model in Geant4 provides a reasonable and efficient calculation of the effective area.

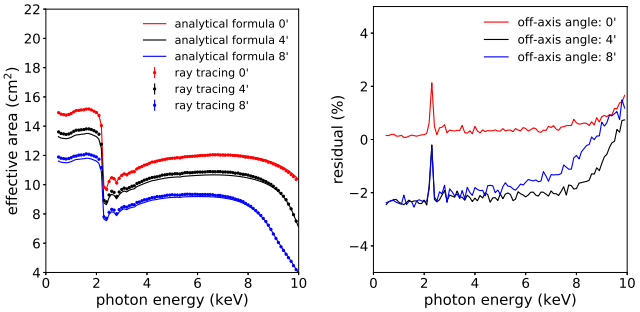


FIG. 3. Effective area curve as a function of photon energy at different off-axis angles for one mirror shell, calculated by ray-tracing model in Geant4 and analytical formula (left). The residual analysis of the results from the ray-tracing model and analytical formula (right).

The calculation of PSF broadening effect is more complicated. For simplicity, the same PSF formula due to figure error is used as slope perturbation function for each photon reflection, whose width has to be changed to account for multiple reflection. It is observed that the shape of PSF can be well reproduced by testing two examples, Gaussian shape PSF and Lorentzian shape PSF, respectively (see figure 4). The Lorentzian shape PSF follows:

$$PSF(\vartheta) = \frac{2|w|}{\pi(w^2 + 4\vartheta^2)} \tag{7}$$

which corresponds to a specific profile error proposed in [26]. What's more, the effect of microroughness can be superposed on the introduced figure errors. It allows a more realistic PSF simulation, which extends the flux out of the core and generates characteristic skirt of photon scattering (see figure 5). According to the Debye-Waller formula, the microroughness effect is energy dependent and sensitive to the shape of PSD. Photon has higher

probability of scattering as the energy increases. For example, photons of 10 keV get an increase of 3.44″ in HEW compared to 1 keV photons, assuming the power index of PSD n = 1.5 and microroughness of PSD $\sigma$ = 0.5 nm.

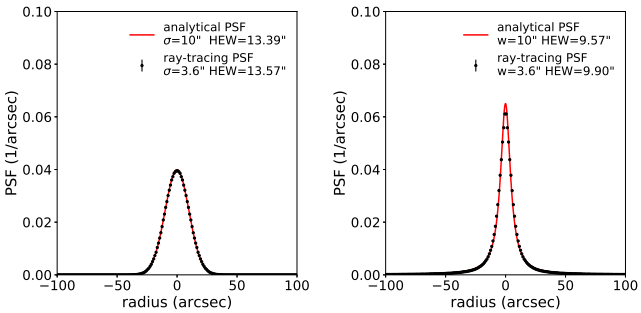


FIG. 4. PSF simulation obtained from ray-tracing model in Geant4 and analytical formula, with Gaussian shape (left) and Lorentzian shape (right) slope perturbation function.

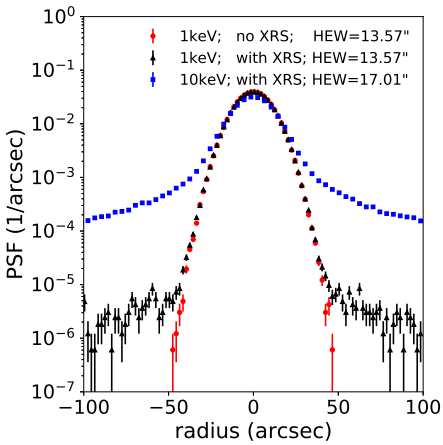


FIG. 5. PSF simulation at different photon energies and surface conditions.

In this section, the geometry and physical models of the interaction between X-rays and matters are validated. The ray-tracing model is able to estimate the effective area with reasonable accuracy. The main characteristics of PSF can be reproduced at different photon energies and surface conditions.

### C. Results

The geometry of one single shell and corresponding physical models are validated in the last section. The nested confocal Wolter-I mirror is then established with 45 shells incorporated. But the spider structure is excluded because it complicates the mirror performances [30], which is out of the extent of the present work. The off-axis angle and energy dependences of focusing performances are presented in this section.

The total effective area with different off-axis angles and corresponding vignetting functions are plotted in figure 6. The current mirror configuration has 828.6 cm$^2$ on-axis effective area at energy 2 keV and 587.2 cm$^2$ at 6 keV. PSF calculation is performed by using Gaussian shape perturbation function ($\sigma$ = 3.6″) and power-law PSD (n = 1.5, $\sigma$ = 0.5 nm). On-axis and off-axis PSF within FOV, as well as corresponding EEF, are plotted in figure 7. It shows insignificant shape change up to 8′. The HEW only increases by less than 2″ as the off-axis angle rises from 0′ to 8′ (see figure 8). The results reported here are consistent with the numbers published in [1].

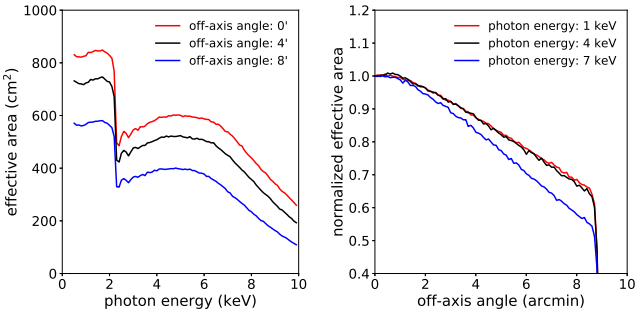


FIG. 6. Effective area curve of 45 mirror shells, depicting clearly the energy dependence (left), while vignetting function shows a clear dependence on the off-axis angle (right).

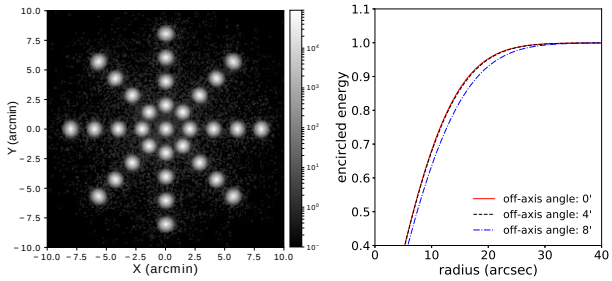


FIG. 7. PSF at different off-axis (ranging from 0′ to 8′) and azimuthal angles (every 45°) within FOV for 1 keV photons (left). $10^6$ photons are simulated for each condition. EEF of the eXTP mirror at different off-axis angles for 1 keV photons (right).

## III. CHARGED PARTICLE RESPONSE

The physical mechanism behind the funnelling effect are reviewed in this section. The first part focuses on the interaction of protons and matters. The second part is dedicated to the low-energy scattering of electrons.

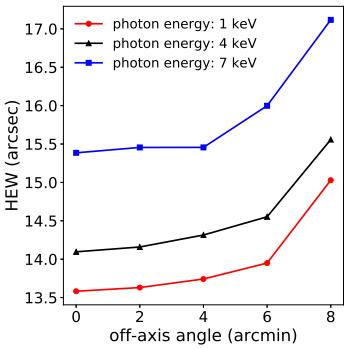


FIG. 8. HEW evolution as a function of the off-axis angle at different photon energies.

### A. Proton Response

#### 1. Physical Models

The funnelling effect was firstly explained that protons undergo numerous scattering and finally escape the reflective layer. Due to the large number of possible interactions, an exact Monte Carlo simulation is very time consuming. The Geant4 toolkit offers several models with different simulation accuracies for multiple scattering process (MSC), including Urban MSC model [13] (G4UrbanMscModel), single scattering model [14] (G4CoulombScattering) and Wentzel-VI MSC model [15] (G4WentzelVIModel).

The Urban MSC algorithm belongs to the "condensed" simulation, which gives the cumulative effect of the angular distribution and spatial distribution after consecutive scattering. For high energy particles and large geometries, it provides satisfactory calculation precision (a few percent for HEP applications) as well as reasonable computation speed [31]. On the contrary, single scattering algorithm is a "detailed" simulation, which samples each elastic scattering with enormous number of stepping, i.e. CPU time. It is usually used in low-energy region and small geometry where Urban MSC algorithm is inapplicable. It gives the best calculation precision and serves as the benchmark for all MSC models. Wentzel-VI MSC algorithm is a mixed model, which uses single and multiple scattering algorithms for hard and soft scattering, respectively. It is now the default MSC model in Geant4 10.5, except for electrons and positrons in the low-energy region.

In addition to the MSC models provided by Geant4, other numerical results have also been used to reproduce the funneling effect [18–20]. Remizovich *et al* [11] have solved the Boltzman transport equation for protons in dense matter and deduced the differential back-scattering coefficient. In order to get rid of the material-dependent parameters, Remizovich *et al* assumed that protons undergoes purely elastic scattering without energy loss in grazing incidence. The material-independent angular distribution R($\psi$,$\chi$) with polar and azimuthal angles is then deduced from the differential back-scattering coefficient, as following:

$$R(\psi,\chi) = \frac{1}{12\pi^2\psi^{1/2}}\Big(\frac{\omega^4}{1+\omega^2} + \omega^3 \arctan\omega\Big) \tag{8}$$

$$\omega = \Big(\frac{3\psi}{\psi^2 - \psi + 1 + (\chi/2)^2}\Big)^{1/2} \tag{9}$$

where $\psi = \frac{\zeta}{\zeta_0}$, $\chi = \frac{\varphi}{\zeta_0}$, $\zeta_0$ is the incident angle, $\zeta$ the scattering polar angle and $\varphi$ the scattering azimuthal angle. Then it can be used in Monte Carlo code to sample the outgoing angles when a proton hits the reflective layer of the mirror.

#### 2. Validation

The Urban MSC model and Wentzel-VI MSC model with default configurations are known that they cannot reproduce the funnelling effect for soft protons in the Wolter-type mirrors, while single scattering model has the capabilities [18–20]. According to the proton trajectories calculated by the single scattering model (see Figure 9), it implies that most of the protons leave the reflective layer very close to the initial incident point (0,0). Thus similar to electron back-scattering problem, it requires very strong limitations in the very first few steps, i.e. fine enough step size, when particles across the boundary. Otherwise the probability to escape the layer is much smaller as particles propagate deeper inside the matter. In case of grazing incidence, the geometry is more special. Even though the average angular deviation for each proton trajectory is small, the lateral displacement can be large enough for protons to leave the boundary, especially at the beginning the trajectory.

Geant4 provides different sets of step limits options [15], including fMinimal, fUseSafety, fUseDistanceToBoundary and fUseSafetyPlus. These options give different simulation accuracies and stabilities at their own costs of CPU time. However, even by using the most strict step limitation (i.e. fUseDistanceToBoundary), Urban MSC model and Wentzel-VI MSC model still cannot reproduce the funnelling effect for soft protons, i.e. almost no proton leaves the refractive layer (see Figure 10). This is probably due to the assumption that the distance to boundary is the half length of the mirror shell (few centimeters) rather than the thickness (few tens of nanometers) due to grazing incidence. In addition, the continuous energy loss process (i.e. ionization) can also impose a limit on the step through SetStepFunctionMuHad interface. The pattern of trajectories changes dramatically with new parameters in SetStepFunctionMuHad. What's more, the most straight forward method to limit maximum step size is to implement a StepMax class as an

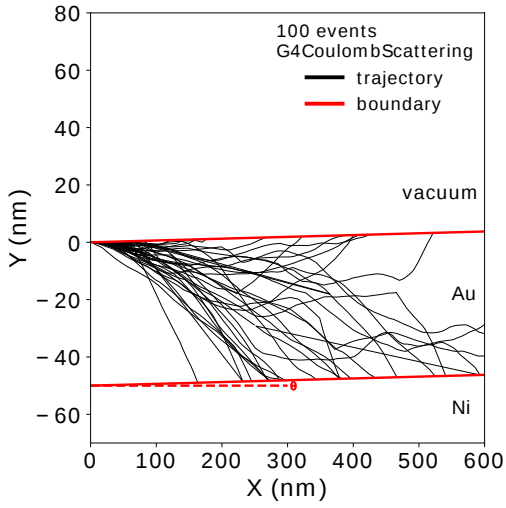


FIG. 9. Proton trajectories in reflecting layer with kinetic energy $E_p = 250$ keV and grazing-incidence angle $\theta = 0.36°$, by using G4CoulombScattering. The incident direction of proton is along the X axis.

artificial physics process, along with G4Region specifying certain logic volume to it. The pattern of proton trajectories with maximum step size of 0.5 nm becomes very similar to the one obtained from the single scattering model at $E_p = 250$ keV. The calculation time is reduced, especially for high energy protons.

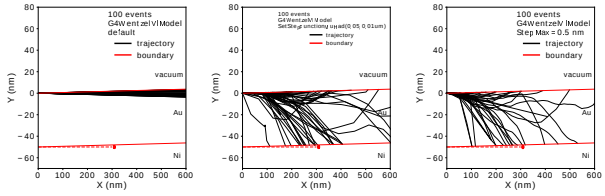

FIG. 10. Proton trajectories in reflecting layer with kinetic energy $E_p = 250$ keV and grazing-incidence angle $\theta = 0.36°$, by using G4WentzelVIModel and different step limitations.

In terms of Remizovich model, several parameters need to be provided by users [18, 20], including energy range, maximum incident angle and binning in the two-dimensional probability density function (PDF). The energy range and maximum incident angle, allowing the activation of the process, are conventionally between 30 keV and 1000 keV and 1°. The sampling of polar and azimuthal angles needs to divide the two-dimensional PDF into discrete bins. Provided 0.1° per bin, it requires 1620000 bins in the full phase space, i.e. from 0° to 90° for polar angle and from -90° to 90° for azimuthal angle. Thus limited angular range can be selected to reduce calculation time, e.g. from 0° to 10° for polar angle and from -10° to 10° for azimuthal angle, depending on the setup configuration.

The simulation results with different scattering models are then quantitatively compared with the experimental measurements [32], which were performed at the Van-de-Graaff accelerator facility of the University of Tübingen. The experimental configurations need to be implemented in simulation for better validation, including the proton beam profile and detection system. The proton energies are broadened after passing through degraders, e.g. 245±32 keV. The proton beam has spatial distribution in the cross section, approximated by Gaussian distribution with $\sigma = 0.21$ mm. The scattered protons are measured by shift-able Silicon surface barrier detectors with a collimator in front to decrease the background. Each detector has detection efficiency almost 100%, energy resolution 10 -20 keV and covers around 1.3 μsr solid angles [32]. A schematic view of the experimental set-up can be seen in figure 11.

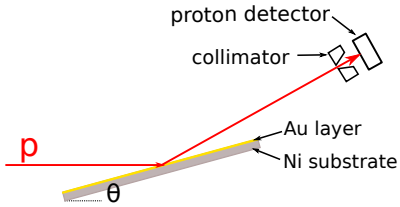


FIG. 11. Schematic view of the experimental set-up for proton scattering measurement at grazing incident angles $\theta$ ranging from 0.3° to 1.2°, adapted from [32]. A single shell sample from eROSITA mirrors was used (10 cm×10 cm), with Gold coating (50 nm) and Nickel substrate (270 μm).

The angular and energy distribution of scattered protons are plotted in figure 12 for model calculations and experimental measurements, respectively (incident $E_p = 250$ keV). The main discrepancy appears at the low scattering angles. G4CoulombScattering and G4WentzelVIModel combined with StepMax ($s_{max} = 0.5$ nm) are able to better reproduce the experimental angular distribution. The default configuration of G4WentzelVIModel cannot reproduce the funnelling effect at all as expected. What's more, the accuracy of G4WentzelVIModel with a fixed maximum step size (e.g. 0.5 nm) varies with the proton energy. For soft protons, e.g. $E_p = 100$ keV, the maximum step size of 0.5 nm is not fine enough for a precise angular distribution generation (see figure 13). Remizovich model overestimates the probability at low scattering angles. It can be used to provide the upper limit of the transmission probability. On the other hand, the energy loss distribution obtained from Geant4 models is significantly lower than that from the measurements, which remains unexplained.

The multiple scattering models with default configurations are conventionally discarded for the explanation of the funnelling effect. In this section, MSC models are validated to have the same capability to reproduce the funnelling effect when the step size is fine enough, e.g.

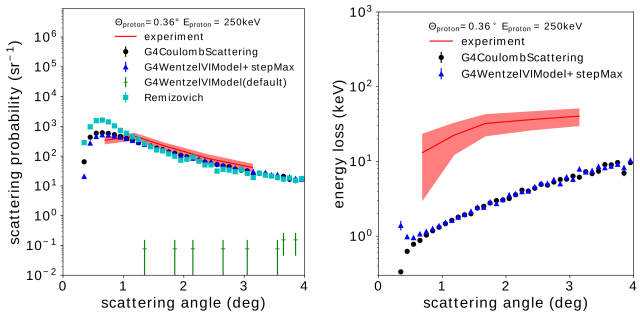


FIG. 12. Comparison of scattering probability (left) between model calculations and experimental measurement, with proton kinetic energy $E_p = 250$ keV and grazing-incidence angle $\theta = 0.36°$. Comparison of energy loss distribution (right) between model calculations and experimental measurement with same conditions.

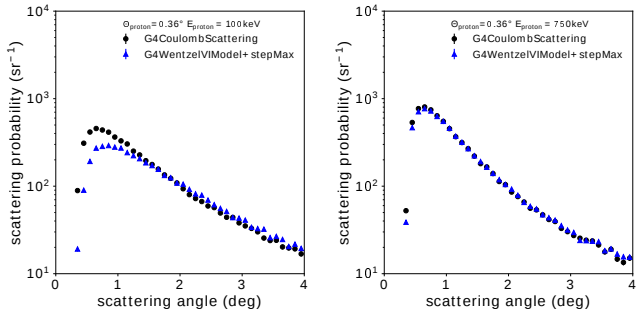


FIG. 13. Scattering probability at different proton energies, $E_p = 100$ keV (left) and $E_p = 750$ keV (right).

maximum step size of 0.5 nm for $E_p > 250$ keV. It provides reasonable accuracy and reduced calculation time compared to the single scattering model, especially in the high-energy region.

## B. Electron Response

### 1. *Physical Models*

The modelling of low-energy electron scattering is a key component in Geant4 toolkit and has drawn a lot of attention, since many physics applications rely on the accuracy of this process, e.g. electron therapy in medical physics. Specific MSC model, Goudsmith-Saunderson (G4GoudsmithSaundersonMscModel), is implemented in Geant4 for low-energy electron scattering. In default, it is used for low-energy region, while Wentzel-VI MSC model for high-energy region. In Goudsmith-Saunderson MSC model, the spatial-angular correlations of electrons for certain step-length are calculated depending on single, multiple or no scattering situation, whose probability is pre-calculated and sampled at each step. It has been demonstrated that Goudsmith-Saunderson MSC model exhibits a reasonable agreement with single scattering model at lower CPU cost [33, 34].

### 2. *Validation*

The validation of low-energy electron scattering is usually performed in terms of the backscattering coefficient [33, 34], defined as the ratio between the number of electron backscattered from the sample surface and the total number of incident electrons. Many experimental measurements in the past have obtained the backscattering coefficient at normal or small incident angles rather than grazing incident angles. And there is also a lack of angular and energy loss distribution. As a result, the validation here for the mirror response of electrons is not straight forward. Single scatter model is taken as a reference because Paolo Dondero *et al* [34] have demonstrated that single scattering model gives the best agreement with the available experimental datasets in terms of the backscattering coefficient above 0.1 keV.

Figure 14 plots the scattering probability and energy loss distribution of scattered electrons within the same experimental configurations as described in the last section (incident $E_{e^-} = 250$ keV). The distributions of proton are also plotted for better comparison. The lowest electron energy is set to be the same for the two models and low enough (50 eV) to avoid any possible effect. The comparison shows that the funnelling effect calculated by the single scattering model is more intense than that by Goudsmith-Saunderson MSC model. The differences are smaller for high-energy electrons, see figure 15. Compared to the scattering probability of protons, the distribution of electrons is much flatten, nearly one order of magnitude lower at small angles, which means that electrons are much less focused by the Wolter-I mirror onto FPDs than protons.

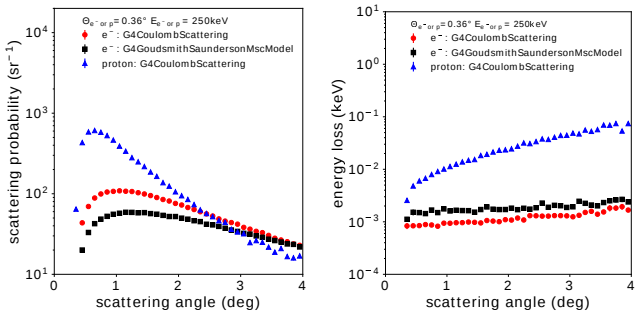


FIG. 14. Comparison of scattering probability (left) and energy loss distribution (right) for the two electron scattering models.

In this section, the default MSC model for electrons (G4GoudsmithSaundersonMscModel) are validated by taking single scattering model as reference. It is able

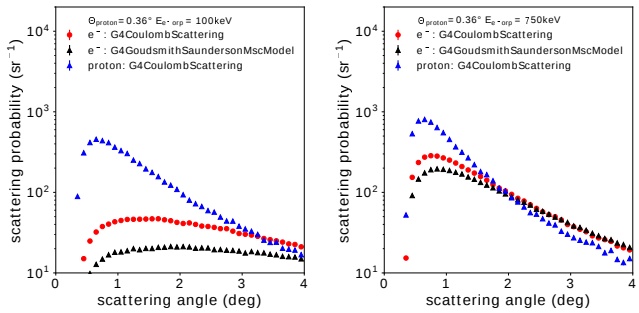


FIG. 15. Scattering probability at different electron energies, $E_{e^-} = 100$ keV (left) and $E_{e^-} = 750$ keV (right).

to reproduce the funnelling effect of electrons in grazing incidence, but with lower scattering probability compared to the single scattering model. Similar to the treatment for protons, the single scattering model can be used for low-energy electrons, while the MSC model for high-energy electrons, e.g. $E_{e^-} > 1$ MeV.

### C. Results

The physics processes behind the funnelling effect are validated in the last section for both protons and electrons. They are now applied to the eXTP optics to simulate the mirror response of charged particles.

The proton response of eXTP mirror is plotted in figure 16, including the transmission probability and energy loss distribution for different incident energies. The transmission probability, defined as the ratio between the number of charged particles reach FPDs (typical area 2.7 × 2.7 cm) and the total number of incident particles on the aperture, decreases exponentially as the off-axis angle rises. However, a bump is observed around 0.6° off-axis angle in all physical models and incident proton energies. This structure corresponds to the protons reaching FPDs that undergo one scattering rather than multiple scattering in the mirror, similar to "straylight". The MSC model combined with StepMax is able to reproduce the distribution of single scattering model at high proton energies, but not in the low-energy region. It implies that more strict step limitation instead of 0.5 nm is needed at $E_p = 100$ keV. In addition, Remizovich model is energy and material independent, and provides the upper limit of the transmission probability.

The energy loss distribution of protons is also plotted in figure 16. Since both model calculations have similar results, i.e. G4CoulombScattering and G4WentzelVIModel combined with StepMax, only the ones from the former model are plotted for better visibility. The slope of the energy loss distribution changes at different off-axis angles. For example, an exponential fit gives slope parameters - 0.37 keV$^{-1}$, - 0.48 keV$^{-1}$, - 0.38 keV$^{-1}$ for 0°, 0.6°, 1.2° off-axis angles respectively, at $E_p = 250$ keV. The softening of the distribution around 0.6° off-axis angle means that small energy loss is favoured, which is corresponding to the decreased number of scattering in mirror.

The same characteristics are observed in the electron response of mirror as well (see figure 17) with a bump appearing around 0.6° off-axis angle in the transmission probability curve. Since electrons are less focused by Wolter-I mirror than protons, the transmission probability is generally few times lower than that of protons. In addition, the energy loss distribution is peaked at very small values with a tail on the right. Consequently, the energy loss of electrons through the mirror can be neglected.

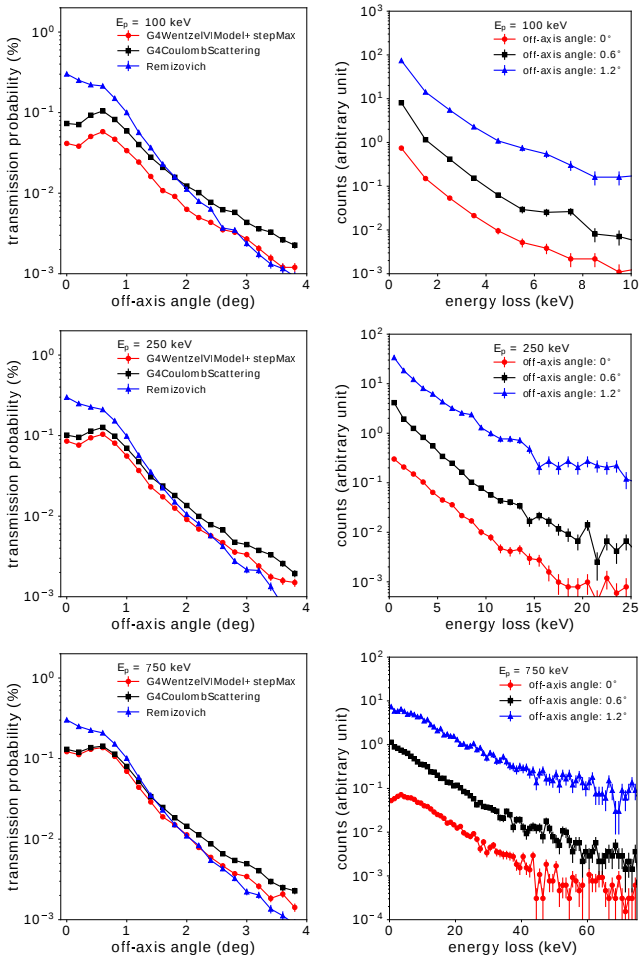


FIG. 16. The proton response of mirror at different incident energies, including the transmission probability and energy loss distribution. The energy loss distribution at different off-axis angles is scaled for better visibility.

In recent update of the mirror design, a Gold layer (100 nm) with an overcoating of Carbon (10 nm) is proposed as the reflective layer. The new design can increase the effective area in collecting X-rays, see details in [35]. The transmission probability for charged particles with

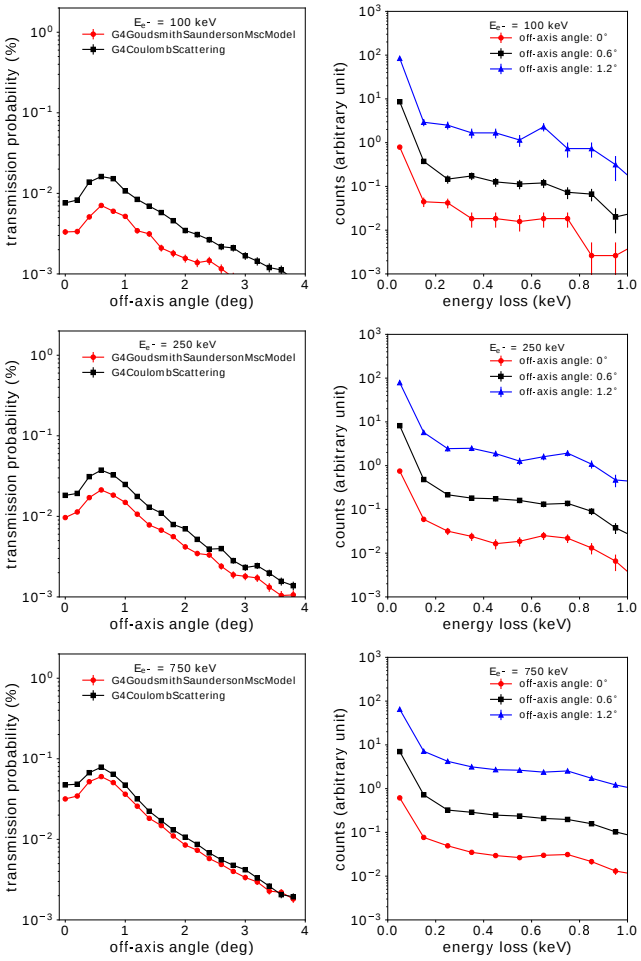


FIG. 17. The electron response of mirror at different incident energies, including the transmission probability and energy loss distribution. The energy loss distribution at different off-axis angles is scaled for better visibility.

new mirror configurations is investigated in this work. Figure 18 shows that the transmission probability is increased by few times. It probably indicates that the materials for the reflective layer with smaller atomic mass enhance the funnelling effect.

## IV. APPLICATION: PRELIMINARY MAGNETIC DIVERTER DESIGN

Charged particles are non-negligible components in the cosmic environment. And the funnelling effect of Wolter-I mirrors focuses charge particles onto FPDs, which can induce performance degradation. Proper magnetic diverter can be implemented at the exit pupil of focusing mirror to reduce the flux of charged particles. Based on the mirror response as discussed in the previous sections, a design of magnetic diverter can be performed directly within the same simulation framework of Geant4. The

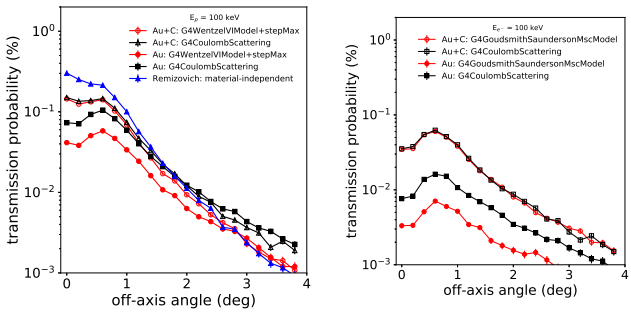


FIG. 18. The transmission probability of protons (left) and electrons (right) respectively, by using different relective layer materials.

current design in this work aims to deflect protons.

In order to avoid X-ray obstruction, 18 spokes of permanent magnets and their dimensions (except for the height) are constrained by the ray-tracing results with the presence of optical spider structure (see figure 19). The magnets are currently placed 15 cm away from the mirror to avoid any possible magnetization or deformation of the mirror components. In the case of eXTP mission, the angular distribution of protons suggests a uniform magnetic induction **B** at different radius, and the requirement of Bl = 392.7 G·cm for minimum deflection angle $\theta_{min} = 0.5°$ at proton energy $E_p = 100$ keV. However, it is difficult to produce a uniform magnetic field in reality. Instead, three Nd-Fe-B magnets are used in each spoke with slightly different dimensions and properties, whose magnetic dipole is oriented on the spider plane to produce an azimuthal magnetic field.

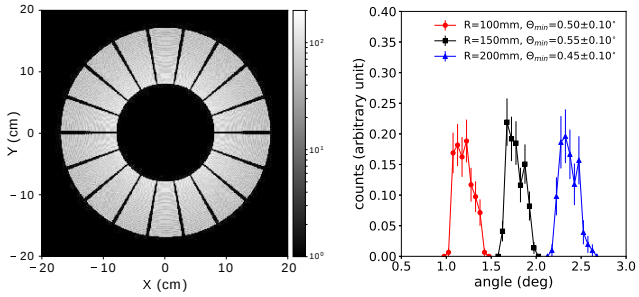


FIG. 19. The spatial distribution of photons with the presence of spider structure, at a plane 15 cm away from the exit pupil of mirror (left). The polar angle distribution of protons that reach FPDs, calculated by G4CoulombScattering at the same plane (right).

The magnetic field is calculated by using the Python3 toolbox magpylib [36], which applies analytical formalism for ideal hard magnets. The magnetic induction **B** field (see figure 20) is then imported into Geant4 to simulate the trajectory of charged particles under field. Figure 20 illustrates that the proton flux in front of FPDs (typical

area 2.7 × 2.7 cm) at energy $E_p$ = 100 keV is decreased by one order of magnitude with the presence of magnetic diverter, regardless of the applied physics list. In addition, the magnetic diverter designed for protons acts as a electron concentrator due to charge difference. However, the magnetic field is so intense for electrons that it shields incident electrons at energy $E_{e^-}$ = 100 keV with ∼100% efficiency.

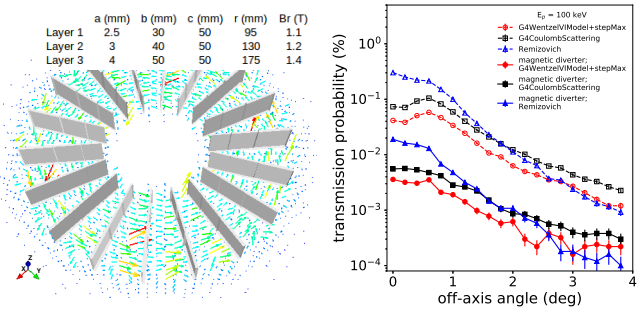


FIG. 20. Magnetic induction **B** field distribution in space (left). The comparison of proton transmission probability with and without the presence of magnetic diverter (right).

## V. CONCLUSIONS

The Wolter-type mirror responses of X-rays and charged particles are investigated in this work. It can help design the payloads of the eXTP mission in detail, e.g. the background estimation and radiation shield optimization. First of all, the geometric model of Wolter-I optics is established and validated in Geant4, with a newly developed geometry class G4Hyperboloid and already existing class G4Paraboloid. It can eliminate the systematic error introduced by conventional geometric approximation.

The physical model for the interaction of X-rays and matters is extended in Geant4. The figure error of large spatial scale and microroughness effect of the surface are taken into account. It provides quick access to the performances of Wolter-I type optics with reasonable accuracy, including effective area and point spread function.

The physical mechanisms behind the funnelling effect of charged particles are discussed. It shows that most of charged particles escape the reflecting layer at the very beginning of the trajectory, requiring fine step size in simulation. Multiple scattering models with proper step limitation are demonstrated to have the capability to reproduce the funnelling effect with reasonable accuracy and calculation cost.

A preliminary design of the magnetic diverter is performed within the same framework of Geant4, by using directly the results of the mirror response. The current magnet configuration can decrease the proton flux at $E_p$ = 100 keV by one order of magnitude and electron flux at $E_{e^-}$ = 100 keV by almost 100%.

## ACKNOWLEDGMENTS

We would like to thank .... We also acknowledge the support from the ... project.

## REFERENCES

[1] S. Zhang, A. Santangelo, M. Feroci, Y. Xu, F. Lu, Y. Chen, H. Feng, S. Zhang, S. Brandt, M. Hernanz, et al., The enhanced x-ray timing and polarimetry missionextp, SCIENCE CHINA Physics, Mechanics & Astronomy 62 (2) (2019) 29502.

[2] L. Raimondi, D. Spiga, Mirrors for x-ray telescopes: Fresnel diffraction-based computation of point spread functions from metrology, Astronomy & Astrophysics 573 (2015) A22.

[3] J. E. Harvey, E. C. Moran, W. P. Zmek, Transfer function characterization of grazing incidence optical systems, Applied optics 27 (8) (1988) 1527–1533.

[4] S. Agostinelli, J. Allison, K. a. Amako, J. Apostolakis, H. Araujo, P. Arce, M. Asai, D. Axen, S. Banerjee, G. . Barrand, et al., Geant4a simulation toolkit, Nuclear instruments and methods in physics research section A: Accelerators, Spectrometers, Detectors and Associated Equipment 506 (3) (2003) 250–303.

[5] E.-J. Buis, G. Vacanti, X-ray tracing using geant4, Nuclear Instruments and Methods in Physics Research Section A: Accelerators, Spectrometers, Detectors and Associated Equipment 599 (2-3) (2009) 260–263.

[6] M. Ozaki, H. Odaka, T. Sato, T. Yasuda, M. Asai, K. Hiragi, T. Mizuno, H. Mori, Y. Terada, A. Furuzawa, A monte carlo simulation framework to study astro-h in-orbit radiation and detector responses based on geant4 toolkit, in: Space Telescopes and Instrumentation 2012: Ultraviolet to Gamma Ray, Vol. 8443, International Society for Optics and Photonics, 2012, p. 844356.

[7] D. Zhao, C. Zhang, W. Yuan, S. Zhang, R. Willingale, Z. Ling, Geant4 simulations of a wide-angle x-ray focusing telescope, Experimental Astronomy 43 (3) (2017) 267–283.

[8] E. Kendziorra, T. Clauss, N. Meidinger, M. Kirsch, M. Kuster, P. Risse, G. D. Hartner, R. Staubert, L. Strueder, Effect of low-energy protons on the performance of the epic pn-ccd detector on xmm-newton, in: X-Ray and Gamma-Ray Instrumentation for Astronomy XI, Vol. 4140, International Society for Optics and Photonics, 2000, pp. 32–41.

[9] D. Lo, J. Srour, Modeling of proton-induced ccd degradation in the chandra x-ray observatory, IEEE Transactions on Nuclear Science 50 (6) (2003) 2018–2023.

[10] O. Firsov, Reflection of fast ions from a dense medium

at glancing angles, in: Soviet Physics Doklady, Vol. 11, 1967, p. 732.
[11] V. Remizovich, M. Ryazanov, I. Tilinin, Energy and angular distributions of particles reflected in glancing incidence of a beam of ions on the surface of a material, Sov. J. Exp. Th. Phys 52 (1980) 225.
[12] B. Aschenbach, Grazing incidence reflection and scattering of mev protons, in: Optics for EUV, X-Ray, and Gamma-Ray Astronomy III, Vol. 6688, International Society for Optics and Photonics, 2007, p. 66880I.
[13] L. Urbán, A model for multiple scattering in geant4, Tech. rep. (2006).
[14] M. H. Mendenhall, R. A. Weller, An algorithm for computing screened coulomb scattering in geant4, Nuclear Instruments and Methods in Physics Research Section B: Beam Interactions with Materials and Atoms 227 (3) (2005) 420–430.
[15] V. Ivanchenko, O. Kadri, M. Maire, L. Urban, Geant4 models for simulation of multiple scattering, in: Journal of Physics: Conference Series, Vol. 219, IOP Publishing, 2010, p. 032045.
[16] O. Kadri, V. Ivanchenko, F. Gharbi, A. Trabelsi, Incorporation of the goudsmit–saunderson electron transport theory in the geant4 monte carlo code, Nuclear Instruments and Methods in Physics Research Section B: Beam Interactions with Materials and Atoms 267 (23-24) (2009) 3624–3632.
[17] B. K. Dichter, S. Woolf, Grazing angle proton scattering: effects on chandra and xmm-newton x-ray telescopes, IEEE Transactions on Nuclear Science 50 (6) (2003) 2292–2295.
[18] V. Fioretti, T. Mineo, A. Bulgarelli, P. Dondero, V. Ivanchenko, F. Lei, S. Lotti, C. Macculi, A. Mantero, A. collaboration, et al., Geant4 simulations of soft proton scattering in x-ray optics, Experimental Astronomy 44 (3) (2017) 413–435.
[19] F. Lei, R. Nartallo, P. Nieminen, E. Daly, H. Evans, P. Truscott, Update on the use of geant4 for the simulation of low-energy protons scattering off x-ray mirrors at grazing incidence angles, IEEE transactions on nuclear science 51 (6) (2004) 3408–3412.
[20] A. Guzmán, E. Perinati, S. Diebold, C. Tenzer, A. Santangelo, A revision of soft proton scattering at grazing incidence and its implementation in the geant 4 toolkit, Experimental Astronomy 44 (3) (2017) 401–411.
[21] H. Wolter, Spiegelsysteme streifenden einfalls als abbildende optiken für röntgenstrahlen, Annalen der Physik 445 (1-2) (1952) 94–114.
[22] H. F. Tschunko, Imaging performance of annular apertures, Applied optics 13 (8) (1974) 1820–1823.
[23] D. T. Attwood, P. Naulleau, K. A. Goldberg, E. Tejnil, C. Chang, R. Beguiristain, P. Batson, J. Bokor, E. M. Gullikson, M. Koike, et al., Tunable coherent radiation in the soft x-ray and extreme ultraviolet spectral regions, IEEE Journal of Quantum Electronics 35 (5) (1999) 709–720.
[24] B. L. Henke, E. M. Gullikson, J. C. Davis, X-ray interactions: photoabsorption, scattering, transmission, and reflection at e= 50-30,000 ev, z= 1-92, Atomic data and nuclear data tables 54 (2) (1993) 181–342.
[25] K. E. Torrance, E. M. Sparrow, Theory for off-specular reflection from roughened surfaces, Josa 57 (9) (1967) 1105–1114.
[26] D. Spiga, L. Raimondi, C. Svetina, M. Zangrando, X-ray beam-shaping via deformable mirrors: Analytical computation of the required mirror profile, Nuclear Instruments and Methods in Physics Research Section A: Accelerators, Spectrometers, Detectors and Associated Equipment 710 (2013) 125–130.
[27] B. Aschenbach, Boundary between geometric and wave optical treatment of x-ray mirrors, in: Optics for EUV, X-Ray, and Gamma-Ray Astronomy II, Vol. 5900, International Society for Optics and Photonics, 2005, p. 59000D.
[28] S. Gougeon, O. Hignette, A. K. Freund, U. Lienert, P. Gondoin, D. de Chambure, Surface characterization of an xmm mandrel at the european synchrotron radiation facility: part ii, in: Multilayer and Grazing Incidence X-Ray/EUV Optics III, Vol. 2805, International Society for Optics and Photonics, 1996, pp. 90–107.
[29] D. Spiga, V. Cotroneo, S. Basso, P. Conconi, Analytical computation of the off-axis effective area of grazing incidence x-ray mirrors, Astronomy & Astrophysics 505 (1) (2009) 373–384.
[30] A. Read, S. Rosen, R. Saxton, J. Ramirez, A new comprehensive 2d model of the point spread functions of the xmm-newton epic telescopes: spurious source suppression and improved positional accuracy, Astronomy & Astrophysics 534 (2011) A34.
[31] J. Apostolakis, A. Bagulya, S. Elles, V. Ivanchenko, O. Kadri, M. Maire, L. Urban, The performance of the geant4 standard em package for lhc and other applications, in: Journal of Physics: Conference Series, Vol. 119, IOP Publishing, 2008, p. 032004.
[32] S. Diebold, C. Tenzer, E. Perinati, A. Santangelo, M. Freyberg, P. Friedrich, J. Jochum, Soft proton scattering efficiency measurements on x-ray mirror shells, Experimental Astronomy 39 (2) (2015) 343–365.
[33] T. Basaglia, M. C. Han, G. Hoff, C. H. Kim, S. H. Kim, M. G. Pia, P. Saracco, Quantitative test of the evolution of geant4 electron backscattering simulation, IEEE Transactions on Nuclear Science 63 (6) (2016) 2849–2865.
[34] P. Dondero, A. Mantero, V. Ivanchencko, S. Lotti, T. Mineo, V. Fioretti, Electron backscattering simulation in geant4, Nuclear Instruments and Methods in Physics Research Section B: Beam Interactions with Materials and Atoms 425 (2018) 18–25.
[35] Mirror module design of x-ray telescopes of eXTP mission, not published yet.
[36] Https://magpylib.readthedocs.io/en/latest/.